RESEARCH ARTICLE | FEBRUARY 28 2024

Enhancing heat transfer in laminar channel flow by tuning the mass distribution of a flexible reed ⊘

Yuzhen Jin (金玉珍) ⓘ ; Chunhui Leng (冷春晖) ⓘ ; Zhaokun Wang (王兆坤) ⓘ ; Xuming Zhang (章旭明) ⓘ ;
Jingyu Cui (崔靖渝) ✉ ⓘ

Check for updates

View Online   Export Citation

Articles You May Be Interested In

Morphology of laminar rheological flow in polygonal ducts

Physics of Fluids (August 2024)

Similarity solutions of a class of unsteady laminar boundary layer

Physics of Fluids (August 2024)

Forced response of a laminar shock-induced separation bubble

Physics of Fluids (September 2014)

AIP Publishing

Physics of Fluids

Special Topics Open for Submissions

Learn More

Enhancing heat transfer in laminar channel flow by tuning the mass distribution of a flexible reed

Yuzhen Jin (金玉珍),[1] (iD) Chunhui Leng (冷春晖),[1] (iD) Zhaokun Wang (王兆坤),[2] (iD) Xuming Zhang (章旭明),[1] (iD) and Jingyu Cui (崔靖渝)[1,a] (iD)

AFFILIATIONS

[1]Key Laboratory of Fluid Transmission Technology of Zhejiang Province, Zhejiang Sci-Tech University, Hangzhou 310018, China
[2]Department of Mechanical Engineering, The Hong Kong Polytechnic University, Kowloon, Hong Kong, China

[a]Author to whom correspondence should be addressed: jingyucui@zstu.edu.cn

ABSTRACT

Recent studies have leveraged wall-mounted flexible reeds to augment heat transfer efficiency in channel flows. In this study, we demonstrate that tuning the reed's mass distribution can substantially elevate this heat transfer enhancement. Numerical simulations incorporating the fluid–structure–thermal interaction are performed to investigate the impact of mass distribution on the reed dynamics and the associated heat transfer augmentation. The results indicate that the mass distribution of the reed significantly affects its motion mode, which, in turn, critically modulates the heat transfer characteristics. The maximum thermal efficiency factor is obtained when the reed's mass is concentrated at its distal end. Furthermore, the enhancement effect of tuning reed's mass distribution on heat transfer efficiency is closely related to the bending stiffness γ. Within the range of bending stiffness considered in this study (0.02–0.14), the effect of tuning the reed's mass distribution on the thermal efficiency factor exhibits a trend of increase–decrease–increase as the bending stiffness increases. At high bending stiffness, simply tuning the reed's mass distribution can increase the channel heat flux and reduce energy loss, thereby achieving the goal of enhancing the thermal efficiency factor. At $\gamma = 0.14$, allocating the reed's mass at its distal end resulted in a notable enhancement, with a thermal efficiency factor surge of 11.1%.

NOMENCLATURE

c_s	Lattice sound speed
D	Cylinder diameter
E_{loss}	Net energy loss
$\bar{E}_{loss}$	Time-averaged net energy loss
$\boldsymbol{F}_{fluid}$	Fluid force
$\boldsymbol{F}_{wall}$	Repulsive force from the wall
$\boldsymbol{F}_\alpha$	External force
f_α	Density distribution function
f_α^{eq}	Equilibrium distribution function
g_α	Temperature distribution function
g_α^{eq}	Equilibrium temperature distribution function
H	Channel height
h	Eulerian grid spacing
s	Lagrangian coordinate
T	Fluid temperature
T_f	Reed temperature
T_w	Wall temperature
T_∞	Far-field fluid temperature
t	Time
$\boldsymbol{U}$	Reed velocity
u	Velocity
u_{in}	Average inlet flow velocity
$\boldsymbol{X}$	Reed position
$\boldsymbol{X}_{wall}$	Wall position
$\boldsymbol{x}$	Fluid position
Nu_θ	Local Nusselt number
L	Reed length
p	Pressure
Pr	Prandtl number
Q_α	Lagrangian heat source
Q_{net}	Net heat flux
$\bar{Q}_{net}$	Time-averaged net heat flux

Greek symbols

γ	Bending stiffness

08 April 2025 07:26:16

ρ	Fluid density
ρ_f	Reed's linear density
μ	Dynamic fluid viscosity
η	Thermal efficiency factor
q	Eulerian heat source
Re	Reynolds number

Subscript

0	Channel without vortex generators

I. INTRODUCTION

Heat transfer enhancement is a crucial research focus within various engineering applications,[1–6] aiming to improve the efficiency and performance of heat exchange equipment. Currently, thermal management in electronic devices relies on various methods, including natural convection cooling, forced air cooling, liquid cooling, semiconductor cooling, and heat pipe cooling. Thermal management techniques based on natural convection heat transfer have gained widespread application in the cooling of electronic circuitry due to their stable performance, high safety, low noise, and relatively low manufacturing costs.

The thermal issues in electronic devices can be simplified as the modeling of heat transfer within channels, where the placement of vortex generators on the channel surfaces can effectively enhance heat transfer. The utilization of rigid vortex generators, such as ribs, cavities, and shaped fins,[7–13] induces different structures of vortices in the channel, promoting thorough mixing of the cold fluid at the channel center with the hot flow near the wall. Thus, the overall heat transfer efficiency in the flow channel is improved. However, the introduction of vortex generators increases the resistance within the channel, leading to pressure drop and consequent energy losses. Therefore, in the assessment of thermal efficiency, it is essential to comprehensively consider both heat transfer rates and the mechanical energy loss due to the pressure drop.

Compared to rigid vortex generators, flexible structures can more effectively enhance the thermal efficiency within channels.[14] Shoele and Mittal[15] studied the impact of reed flow-induced vibrations placed at the channel center on convective heat transfer. The simulation results indicated that vibrating reed significantly increased the average heat flux in the channel. The study also explored the influence of reed material properties on vibration dynamics and heat transfer. Material variations resulted in various vibration characteristics, and it was found that heat transfer efficiency is more closely related to the reed's inertia rather than its bending stiffness. Research involving various Reynolds number (Re) and channel widths indicates that when there is an interaction between the reed and the channel wall, the boundary layer is disrupted, leading to maximum heat transfer performance while at the same time avoiding the generation of strong vortices. In the investigation conducted by Lee et al.,[16] the immersed boundary method was employed. They explored how vertically clamped flexible flags in a heated channel impact heat transfer efficiency and its mechanism in Poiseuille channel flow. The analysis revealed that, in the flapping mode, vortices shed from the flexible flags merged into a single coherent vortex structure, disrupting the thermal boundary layer and enhancing heat exchange in the wake current. The study also examined different parameters such as bending stiffness, channel width, and

Reynolds number, providing the optimal parameter set for vertically clamped flexible flags to enhance heat transfer.

The aforementioned studies focused on symmetrically placing flexible flags on the upper and lower channel walls. Subsequently, research[17] delved into the study of non-symmetric flexible flags in the channel. This study described a system composed of flexible flags in an asymmetric configuration (FAC) with respect to the channel centerline. The results showed that, compared to flags in symmetric configurations (FSC), FAC produced a reverse Karman vortex street, promoting heat exchange in the wake current to a greater extent. Additionally, the smaller cross-sectional height of FAC's flexible flags compared to FSC reduced channel pressure drop, minimizing the mechanical energy loss, and significantly improving heat transfer efficiency. Chen et al.[18] investigated the flapping behavior of multiple flexible flags in the channel and their impact on heat transfer performance. The study explored the influence of multiple flexible flags, symmetrically and asymmetrically configured along the channel center. Consistent with previous research, heat transfer was more favorable in the case of asymmetric configurations. Then, Chen et al.[19] explored the flapping dynamics of vertically clamped three-dimensional flexible flags in an oncoming Poiseuille flow by using the immersed boundary method. In the study by Jeong et al.,[20] a heat transfer system is proposed as a combination of two symmetrically wall-mounted flexible flags and a confined cylinder positioned in an upstream region of the flags. Their results showed that the optimal performance of the present system is greater than the system with only the two flags. Placing multiple flexible flags in the channel will increase the overall quality of the device. In order to avoid the increase in mechanical energy loss in the channel, Park et al.[21] used a flexible flag with an inclination angle to promote fluid mixing and increase heat transfer. In recent years, many studies[22–24] have focused on the position, initial state, and number of flexible flags. Goza[25] tried to change the flexible flag's properties to enhance heat transfer, they studied flow-induced flapping of an inverted flag with non-uniform stiffness distribution. They investigate the effect of structural nonuniformity in altering the FSI dynamics compared with the uniform-stiffness scenario that have been thoroughly characterized and demonstrate that the FSI dynamics mirror those of a uniform-stiffness flag with an appropriately defined effective stiffness.

Building upon previous research, and Inspired by the research of Goza,[25] this study employs the immersed boundary-lattice Boltzmann method (IB-LBM) to tune the mass distribution of flexible reeds. The research investigates the vibrational characteristics of flexible reeds and their impact on heat transfer efficiency under different mass distributions. The results indicate that when the mass is concentrated at the distal end of the reed, the heat transfer efficiency reaches its maximum. Subsequently, a comparison is made between the scenario of uniform mass distribution and the case where the mass is concentrated at the distal end of the reed. The analysis covers reed oscillation, channel heat flux, energy loss, and heat transfer efficiency. The study further explores the influence of changing mass distribution on heat transfer efficiency under various bending rigidities within the range of 0.02 to 0.14.

II. PROBLEM DESCRIPTION

The computational domain and boundary conditions considered in this study are illustrated in Fig. 1(a). The length of reeds is defined
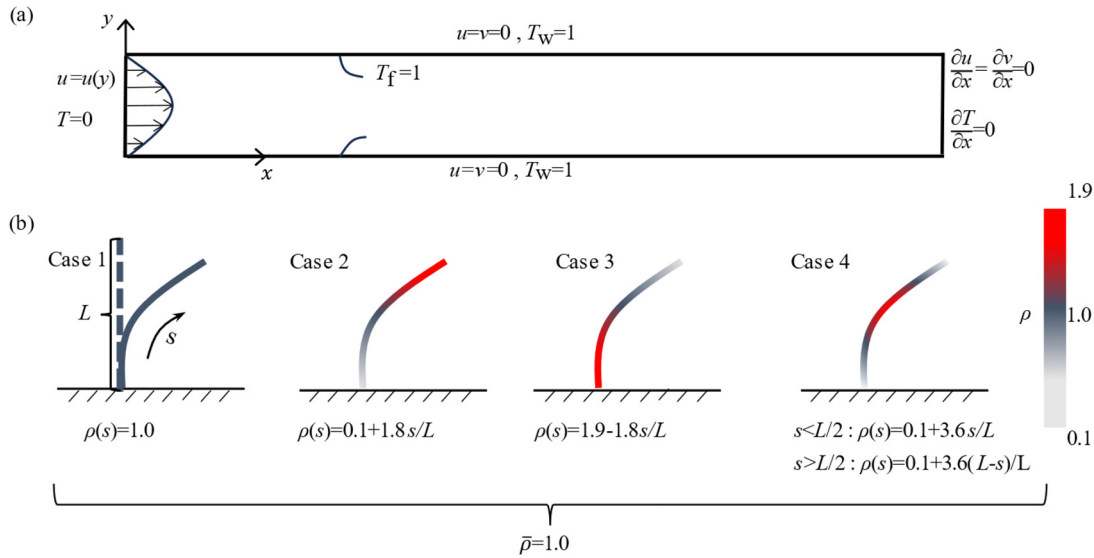
08 April 2025 07:26:16

FIG. 1. (a) Schematic diagram of the computational domain. (b) Schematic diagram of the four tuning schemes.

by L, and the channel dimensions are $4L \times 32L$. The inlet temperature is set to 0, while the temperatures of the walls and reed are set to 1.

The Re of the flow field is defined as

$$Re = \frac{\rho u_{in} L}{\mu}, \quad (1)$$

where u_{in} is the average velocity of the channel inlet and ρ and μ are the density and viscosity of the flow field. In the simulations of this paper, we set Re of the flow field to 400. The basal end of the reed is fixed at 1/4 of the channel length from the inlet, and the distal end is free to move. A parabolic profile is specified at the channel inlet, the no-slip condition is imposed at the channel walls. A fully-developed boundary condition is set for the velocity and temperature at the outlet boundary. The primary objective of this paper is to investigate the influence of reed's mass distribution on channel heat transfer. To achieve this, the reed's mass is strategically tuned using the following four schemes, as depicted in Fig. 1(b): Case 1 represents a uniform distribution of reed mass with a linear density of 1 at each point; case 2 represents a uniform increase in reed density from the basal end to the distal end; case 3 represents a uniform decrease in reed density from the basal end to the distal end; and case 4 represents maximum density at the center of the reed, uniformly decreasing toward both ends. The above four cases always keep the average linear density of the reed constant.

The nondimensionalization of the parameters used in this paper (time t, the linear density of the reed ρ_f, the bending stiffness of the reed k_b, temperature T, position x and y) is given as follows:

$$t^* = \frac{t u_{in}}{L}, \quad \rho_f^* = \frac{\rho_f}{\rho L}, \quad \gamma = \frac{k_b}{\rho u_{in}^2 L^3},$$

$$T^* = \frac{T}{T_w - T_\infty}, \quad x^* = \frac{x}{L}, \quad y^* = \frac{y}{L}, \quad (2)$$

where the fluid density ρ is set to 1, the wall temperature T_w is set to 1, and the temperature T_∞ at infinity is set to 0.

III. MATHEMATICAL MODEL

A. Reed motion

This study employs the filament model to model the motion of the flexible reed. The model is first introduced by Peskin and McQueen[26] for simulating the flapping motion of massless filament (such as neutrally buoyant heart valve) and then improved by other scholars by considering the effect of the boundary mass. This model is different from the classic or generalized nonlinear Euler–Bernoulli models. One of the distinguishing features of this model is the introduction of geometric nonlinearity through inhomogeneous tension. This allows for the effective handling of elastic moving boundaries, particularly in scenarios involving large deformations. The model's robustness and versatility have led to its extensive application in the realm of fluid–flexible–structure interactions,[27–30] and fluid–structure–thermal interaction problems similar to ours.[16,18,31] Therefore, this study chooses this model to simulate the motion of a flexible reed in a two-dimensional channel. When the bending stiffness of the reed is small, large deflections may be caused, and the reed may collide with the wall. To avoid penetration, a short-range repulsive force F_{wall} is introduced in our model to handle the collision between the reed and wall. In this case, the equation of motion of the reed is given by[32,33]

$$\rho_f \frac{\partial^2 X}{\partial t^2} = \frac{\partial}{\partial s}\left[T(s)\frac{\partial X}{\partial s}\right] - k_b \frac{\partial^4 X}{\partial s^4} + F_{fluid} + F_{wall}, \quad (3)$$

where the left-hand side of Eq. (3) represents the inertial force acting on the reed nodes, $k_b \frac{\partial^4 X}{\partial s^4}$ on the right side of the equation is the bending force on the reed node, F_{fluid} is the fluid force applied to the reed node, $\frac{\partial}{\partial s}\left[T(s)\frac{\partial X}{\partial s}\right]$ is the tensile force on the reed node, F_{wall} is the force exerted by the wall on the reed to prevent the reed from penetrating the wall, X represents the position vector of the reed, and s is the Lagrange coordinate along its length. Here, ρ_f is the reed's linear density, and k_b is the bending stiffness.

The tension $T(s)$ is given by

$$T(s) = k_s \left[\left(\frac{\partial \boldsymbol{X}}{\partial s} \cdot \frac{\partial \boldsymbol{X}}{\partial s} \right)^{\frac{1}{2}} - 1 \right], \tag{4}$$

where k_s is the stretch coefficient.

The reed is discretized by $N+1$ equally spaced Lagrange nodes $\boldsymbol{X}(s_i, t)$, where $i = 0, 1, \ldots, N$. The right-hand side of Eq. (3) can be discretized in space using central differencing:

$$\rho_f \frac{\partial^2 \boldsymbol{X}}{\partial t^2} = \frac{T_{i+\frac{1}{2}} \left[\frac{\partial \boldsymbol{X}}{\partial s} \right]_{i+\frac{1}{2}} - T_{i-\frac{1}{2}} \left[\frac{\partial \boldsymbol{X}}{\partial s} \right]_{i-\frac{1}{2}}}{\Delta s}$$
$$- k_b \frac{\boldsymbol{X}_{i+2} - 4\boldsymbol{X}_{i+1} + 6\boldsymbol{X}_i - 4\boldsymbol{X}_{i-1} + \boldsymbol{X}_{i-2}}{\Delta s} + \boldsymbol{F}_{\text{fluid}} + \boldsymbol{F}_{\text{wall}}, \tag{5}$$

where $\frac{\partial \boldsymbol{X}}{\partial s}$ is the tangent vector, and the subscript i denotes the ith reed node:

$$\left[\frac{\partial \boldsymbol{X}}{\partial s} \right]_{i+\frac{1}{2}} = \frac{\boldsymbol{X}_{i+1} - \boldsymbol{X}_i}{\Delta s}. \tag{6}$$

The tension of the reed is approximated as

$$T_{i+\frac{1}{2}} = k_s \left(\left| \frac{\boldsymbol{X}_{i+1} - \boldsymbol{X}_i}{\Delta s} \right| - 1 \right). \tag{7}$$

The repulsive force from the wall to the reed is evaluated by[27]

$$\boldsymbol{F}_{\text{wall}} = \sum_{\boldsymbol{X}} \sigma_h(\boldsymbol{x} - \boldsymbol{X}) \frac{\boldsymbol{X} - \boldsymbol{X}_{\text{wall}}}{|\boldsymbol{X} - \boldsymbol{X}_{\text{wall}}|} d\boldsymbol{X}, \tag{8}$$

where $\boldsymbol{X}_{\text{wall}}$ is the wall position, $d\boldsymbol{X}$ is represents the Lagrangian grid spacing, and the Dirac delta function σ_h is defined as

$$\sigma_h(\boldsymbol{x} - \boldsymbol{X}) = \frac{1}{h^2} \varnothing \left(\frac{x - X}{h} \right) \varnothing \left(\frac{y - Y}{h} \right). \tag{9}$$

The expression for $\varnothing(r)$, proposed by Peskin,[34] is given by

$$\varnothing(r) = \begin{cases} \frac{1}{4} \left(1 + \cos \left(\frac{\pi |r|}{2} \right) \right), & |r| \leq 2 \\ 0, & \text{else} \end{cases}. \tag{10}$$

B. Flow field and temperature field solver

The incompressible fluid flow was governed by the continuity equation and the Navier–Stokes (NS) equations,

$$\nabla \cdot \boldsymbol{u} = 0, \tag{11}$$

$$\frac{\partial \boldsymbol{u}}{\partial t} + \boldsymbol{u} \cdot \nabla \cdot \boldsymbol{u} = -\nabla p + \frac{1}{Re} \nabla^2 \boldsymbol{u} + \boldsymbol{f}. \tag{12}$$

The temperature described on the Eulerian coordinates was governed by the thermal energy equation,

$$\frac{\partial T}{\partial t} + \boldsymbol{u} \cdot \nabla \cdot T = \frac{1}{Re \cdot Pr} \nabla^2 T + \boldsymbol{q}. \tag{13}$$

In this study, Eqs. (11)–(13) are solved by the lattice Boltzmann method (LBM). To solve both the flow and temperature fields, the

two-distribution-function approach by Guo *et al.*[35] is utilized. This approach solves two independent LBGK equations to obtain the velocity and temperature fields, which are then coupled into a unified system. To enhance numerical stability, the flow field utilizes the multi-relaxation time (MRT) collision model. The D2Q9 lattice model was adopted to solve the flow dynamics and temperature field.

The evolution equation of LBM with an external force term is given by[36]

$$f_\alpha(\boldsymbol{x} + \boldsymbol{e}_\alpha dt, t + dt) = f_\alpha(\boldsymbol{x}, t) + \boldsymbol{M}^{-1} \boldsymbol{S} \left[\boldsymbol{M}_\alpha^{\text{eq}}(\boldsymbol{x}, t) - \boldsymbol{M}_\alpha(\boldsymbol{x}, t) \right]$$
$$+ \left(1 - \frac{\boldsymbol{S}}{2} \right) \boldsymbol{F}_\alpha(\boldsymbol{x}, t), \tag{14}$$

where the external force term $\boldsymbol{F}_\alpha$ is defined as

$$F_\alpha = \left(1 - \frac{\boldsymbol{S}}{2} \right) \frac{(\boldsymbol{e}_\alpha - \boldsymbol{u}) f(\boldsymbol{x}, t)}{\rho c_s^2} f_\alpha^{\text{eq}}(\boldsymbol{x}, t), \tag{15}$$

where f_α represents the density distribution function, ρ is the density of the fluid, c_s denotes the lattice speed of sound, $\boldsymbol{M}$ is the transformation matrix, and $\boldsymbol{S}$ is the relaxation matrix.

The equilibrium distribution function f_α^{eq} is chosen as

$$f_\alpha^{\text{eq}}(\boldsymbol{x}, t) = \omega_\alpha \rho \left[1 + \frac{\boldsymbol{e}_\alpha \cdot \boldsymbol{u}}{c_s^2} + \frac{(\boldsymbol{e}_\alpha \cdot \boldsymbol{u})^2}{2c_s^4} - \frac{\boldsymbol{u}^2}{2c_s^2} \right]. \tag{16}$$

The macro quantities in LBM can be conveniently calculated as follows:

$$\rho = \sum_\alpha f_\alpha, \tag{17}$$

$$\boldsymbol{u} = \frac{1}{\rho} \left(\sum_\alpha f_\alpha \boldsymbol{e}_\alpha + \frac{1}{2} \boldsymbol{f} dt \right). \tag{18}$$

The main concept of the MRT-LBM is to decouple the relationship between velocity and density by introducing a collision matrix, enabling the simulation of multiscale phenomena. The stability and accuracy of MRT-LBM surpass traditional LBM due to the ability to tailor the dynamic characteristics, such as viscosity and velocity response, through appropriate selection of collision matrix values, depending on the fluid and problem type.

In the two-distribution-function approach, the temperature evolution equation with heat source is given by[37]

$$g_\alpha(\boldsymbol{x} + \boldsymbol{e}_\alpha dt, t + dt) = g_\alpha(\boldsymbol{x}, t) - \omega_g \left[g_\alpha(\boldsymbol{x}, t) - g_\alpha^{\text{eq}}(\boldsymbol{x}, t) \right] + Q_\alpha dt, \tag{19}$$

where the heat source term Q_α is given by

$$Q_\alpha = \left(1 - \frac{\omega_g}{2} \right) \omega_\alpha q. \tag{20}$$

The equilibrium distribution function $g_\alpha^{\text{eq}}(x, t)$ is calculated as

$$g_\alpha^{\text{eq}}(\boldsymbol{x}, t) = \omega_\alpha T \left[1 + \frac{\boldsymbol{e}_\alpha \cdot \boldsymbol{u}}{c_s^2} + \frac{(\boldsymbol{e}_\alpha \cdot \boldsymbol{u})^2}{2c_s^4} - \frac{\boldsymbol{u}^2}{2c_s^2} \right]. \tag{21}$$

The temperature T is computed through the new distribution function g_α, with $T = \sum_\alpha g_\alpha + \frac{1}{2} q dt$. The heat flux q at the Eulerian point is determined by the Lagrange point heat flux Q,

$$q(\boldsymbol{x}) = \sum_{X} Q(\boldsymbol{X}) D(\boldsymbol{x} - \boldsymbol{X}) \mathrm{d}\boldsymbol{X}, \tag{22}$$

$$Q(\boldsymbol{X}) = 2(T_f - T(\boldsymbol{X})) \frac{\mathrm{d}\boldsymbol{x}}{\mathrm{d}t}, \tag{23}$$

where T_f represents the specified reed temperature.

C. Fluid–structure–thermal interaction

In this study, the coupled fluid–structure interaction of reeds and the flow field is addressed using the momentum exchange-based immersed boundary method.[38] In this approach, the distribution function f at each boundary node of the reeds is obtained by interpolating through a smooth Dirac function denoted as σ_h,

$$f_\alpha(\boldsymbol{X}, t) = \sum_{\boldsymbol{x}} f_\alpha(\boldsymbol{x}, t) \sigma_h(\boldsymbol{x} - \boldsymbol{X}) \mathrm{d}x, \tag{24}$$

where $\sum_{\boldsymbol{x}}$ represents the sum over all Eulerian grid points and $\mathrm{d}x$ denotes the Eulerian grid spacing.

The reed boundaries are set with a no-slip condition, and the distribution function at the reed boundaries is computed using a bounce-back scheme,

$$f_{-\alpha}(\boldsymbol{X}, t + \mathrm{d}t) = f_\alpha(\boldsymbol{X}, t) - 2\omega_\alpha \rho \frac{\boldsymbol{e}_\alpha \boldsymbol{U}(\boldsymbol{X}, t)}{c_s^2}, \tag{25}$$

where $-\alpha$ represents the opposite direction of α and $\boldsymbol{U}(\boldsymbol{X}, t)$ denotes the velocity of the reed nodes. The force exerted by the fluid on the reeds is calculated using the momentum exchange method,

$$\boldsymbol{F}_{\mathrm{fluid}}(\boldsymbol{X}, t) = \boldsymbol{e}_\alpha \sum_\alpha \left(f_{-\alpha}(\boldsymbol{X}, t + \mathrm{d}t) - f_\alpha(\boldsymbol{X}, t) \right). \tag{26}$$

The force exerted by the reeds on the fluid is determined similarly through interpolation,

$$f(\boldsymbol{x}, t) = \boldsymbol{e}_\alpha \sum_{\boldsymbol{X}} \boldsymbol{F}_{\mathrm{fluid}}(\boldsymbol{X}, t) \delta_h(\boldsymbol{x} - \boldsymbol{X}) \mathrm{d}\boldsymbol{X}, \tag{27}$$

where $\mathrm{d}\boldsymbol{X}$ represents the Lagrange grid spacing and $\sum_{\boldsymbol{X}}$ denotes the sum over all Lagrange grid points.

IV. VALIDATIONS

The code utilized in this study to simulate the fluid–structure interaction problem between reed and fluid has been rigorously validated in our previous research.[39–41] Therefore, in this section, the recently incorporated heat transfer and thermal boundary components are validated through the simulation of thermal disturbance around a cylindrical obstacle. The geometric model and boundary conditions for this case are illustrated in Fig. 2, where the cylinder has a diameter D, the grid spacing is $\mathrm{d}x = \mathrm{d}y = 1$, the time step is $\mathrm{d}t = \mathrm{d}x$, the inlet velocity is U, the temperature is $T = 0$, and the boundary temperature of the cylinder is $T_w = 1$. The simulation is conducted for three Reynolds numbers (Re: 10, 20, and 40), and the Nusselt numbers Nu are calculated and compared with literature values.[42]

Figure 3 illustrates the temperature distribution of turbulent flow around a heated cylindrical body at different Reynolds numbers, concurrently comparing the calculated Nusselt number with values from the referenced literature. In Figs. 3(a)–3(c), the temperature distribution under various Reynolds numbers (Re) is depicted. It is observed
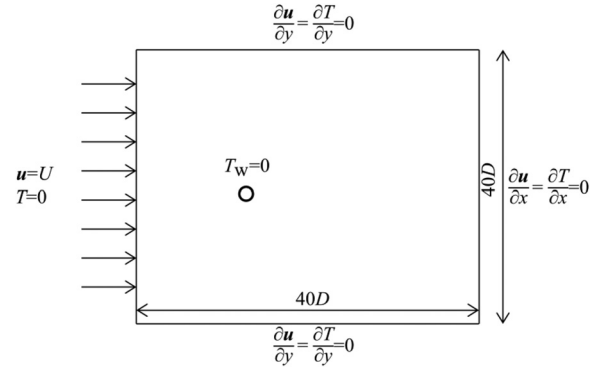

FIG. 2. Schematic diagram of the thermal cylindrical flow calculation domain.

that with an increase in Reynolds number, the heat transfer rate also increases, and simultaneously, the thermal boundary layer gradually diminishes. This aligns with the expected physical behavior, as higher Reynolds numbers typically signify more intense turbulent motion, leading to more efficient heat transfer. Figure 3(d) showcases the local Nusselt number Nu_θ evaluated at the cylinder surface, computed as

$$Nu_\theta = -\frac{D}{T_w - T_\infty} \frac{\partial T(s, t)}{\partial \boldsymbol{n}}\Big|_\theta, \tag{28}$$

where θ represents the angle between the line connecting a point on the surface of the cylinder to the center of the circle and the negative x-axis.

The results indicate a substantial agreement between the calculated Nu_θ and values from the literature, affirming the program's commendable accuracy and reliability in simulating turbulent heat flow around a cylindrical body.

In order to ensure that the grid spacing used in our simulations is sufficient for simulating this problem, a grid independence study has been conducted which covers four sets of grid resolutions. The accuracy of the simulation was determined by comparing the channel thermal efficiency factor η of different grid spacings,

$$\eta = \frac{\bar{Q}_{\mathrm{net}}}{\bar{Q}_{0,\mathrm{net}}} \times \left(\frac{\bar{E}_{0,\mathrm{loss}}}{\bar{E}_{\mathrm{loss}}} \right)^{\frac{1}{3}}, \tag{29}$$

where $\bar{Q}_{\mathrm{net}}$ is the average net heat flux of the channel and $\bar{E}_{\mathrm{loss}}$ is the average energy loss and the subscript 0 indicates that the value is measured without additional devices placed in the channel. The net heat flux Q_{net} and energy loss E_{loss} of the channel can be calculated by the following formula:

$$Q_{\mathrm{net}} = \int_0^H \left[(\boldsymbol{u}T)_{\mathrm{out}} - (\boldsymbol{u}T)_{\mathrm{in}} \right] \mathrm{d}y, \tag{30}$$

$$E_{\mathrm{loss}} = \int_0^H \left[(\boldsymbol{u}p)_{\mathrm{in}} - (\boldsymbol{u}p)_{\mathrm{out}} \right] \mathrm{d}y, \tag{31}$$

where the subscripts in and out indicate channel inlet and outlet.

$\bar{Q}_{\mathrm{net}}$, $\bar{E}_{\mathrm{loss}}$, and η are evaluated a constant time step when the reed experience at least 30 flapping cycles. The simulation results are shown in Table I. The thermal efficiency factor of the channel can
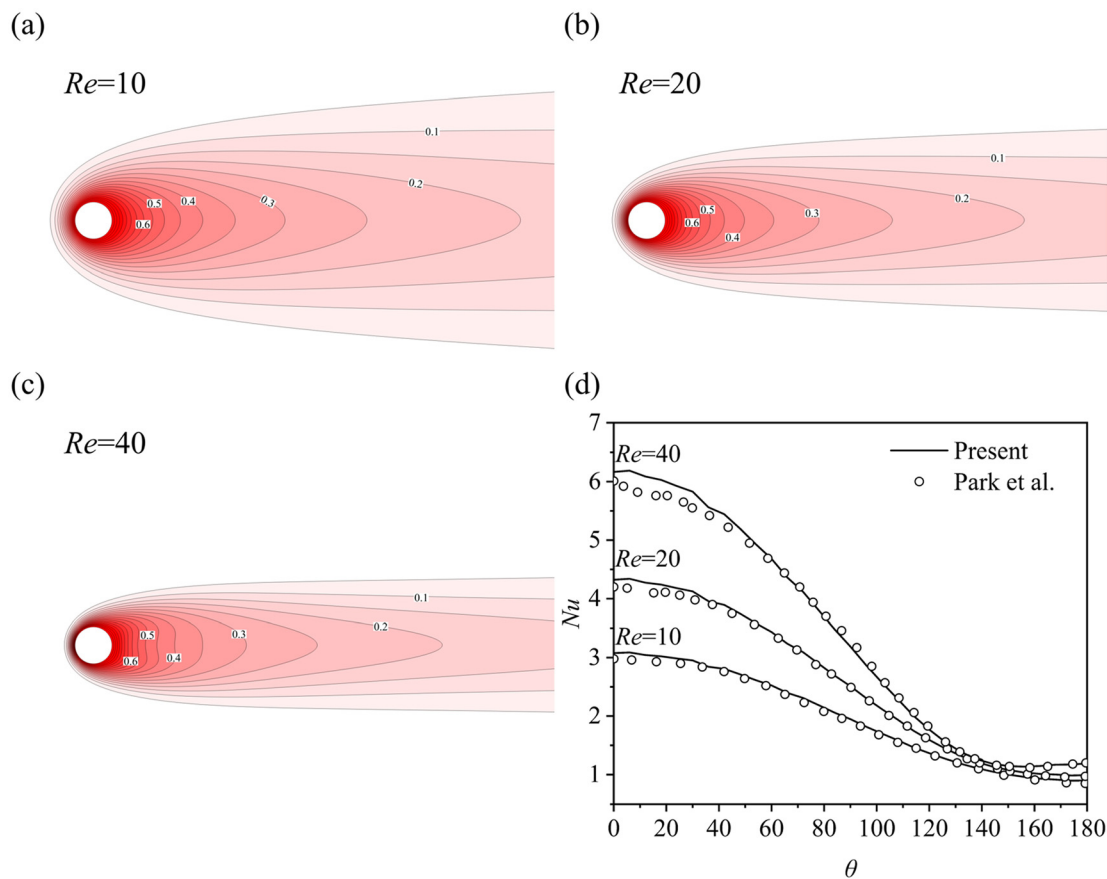
(a)

Re=10

(b)

Re=20

(c)

Re=40

(d)

FIG. 3. (a)–(c) Contours of temperature for the flow past a heated rigid cylinder with the isothermal boundary condition. (d) The local Nusselt number along the rigid circular cylinder for the isothermal boundary condition.

TABLE I. Grid independence verification.

Grid spacing dh	Thermal efficiency factor η	Relative error (%)
1/25	1.687 62	28.7
1/50	1.321 91	0.88
1/75	1.311 86	0.11
1/100	1.310 37	…

basically be accurately obtained when the grid spacing is 1/75, so this grid spacing is chosen for the subsequent numerical simulations.

V. RESULTS AND DISCUSSION

A. Tuning the mass distribution of the reed

To investigate the impact of the four mentioned mass distribution patterns of flexible reeds on their motion characteristics and heat transfer efficiency, simulations were conducted under the condition of $\gamma = 0.06$. The study explored the motion of flexible reeds under four different mass distribution scenarios and the variations in the flow field and temperature field within the channel. The results revealed significant differences in the motion of the reeds under the four conditions,

each exerting distinct influences on the temperature field. In Fig. 4, the changes in the range of reed motion and the *y*-axis coordinates at the distal end are illustrated. Notably, concentrating mass at the distal end visibly expanded the range of motion, transforming the motion pattern from regular oscillation to irregular oscillation. Conversely, in the other two mass distribution cases, the reed's mass is concentrated in the middle of the basal end. The mass concentration point is closer to the channel boundary layer, with sections with smaller mass in the region of higher flow velocity at the center. Thus, the reed could not resist the effects of the flow field. As the flow field evolved, the motion pattern of the reeds gradually transformed into the fully deflective mode.

Distinct motion patterns also led to variations in temperature distribution within the channel. Figure 5 illustrates the temperature distribution within the channel under the four scenarios. It is evident from the figures that tuning the mass distribution affected the shedding of vortices, consequently altering the temperature distribution within the channel. When the mass of the reed is concentrated at the basal end or in the middle, the temperature distribution closely resembles that of a rigid body placed on the wall due to its fully deflective motion pattern, which is unfavorable to enhancing heat transfer efficiency. In this case, only the temperature around the reed is affected, and the effect on the channel outlet is extremely weak. Specifically, when the mass is
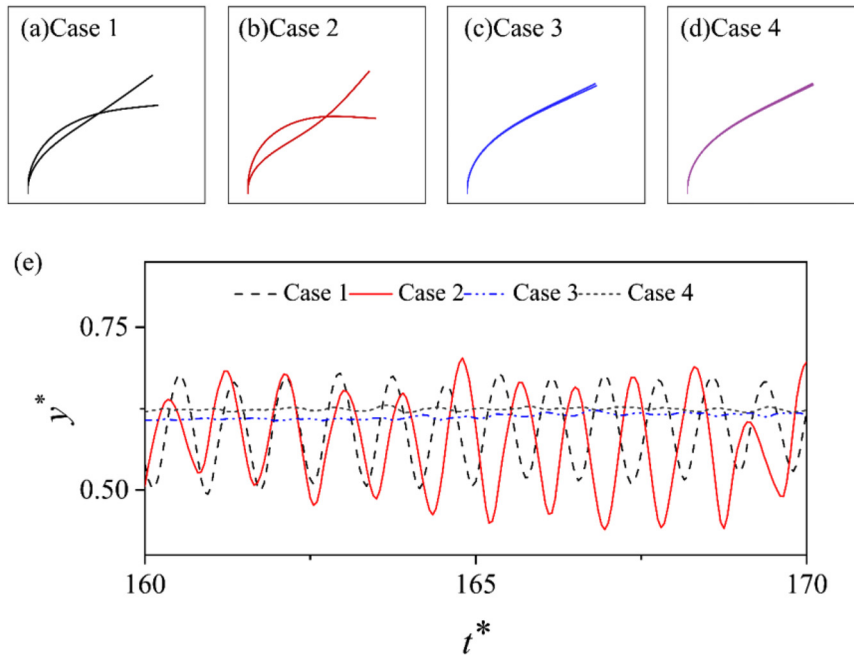
FIG. 4. (a)–(d) The range of motion of the reed under four different mass distributions, and (e) the y coordinates of the reed's distal end.

concentrated in the middle as in case 4, only the temperature near the wall is affected, and the cold flow in the middle of the channel is completely unaffected. When the mass is concentrated at the basal end, such as in case 3, the vortices generated at the tail of the reed dissipate after merging. The temperature diagram illustrates that the dissipation of vortices promotes the mixing of the hot flow along the wall and the cold flow in the center of the channel, significantly impacting the center of the channel compared to Case 1. It can also be seen from the velocity vector diagram that case 3 has the greatest influence on the channel center. However, its low vortex shedding frequency limits its ability to continuously enhance heat transfer.

To accurately assess the impact of various mass distributions on heat transfer efficiency, we calculated the channel-averaged net heat flux ($\bar{Q}_{net}$), average mechanical energy loss ($\bar{E}_{loss}$), and thermal efficiency factor (η). The specific data are presented in Table II. Under the condition of $\gamma = 0.06$, optimal heat transfer efficiency was attained when the mass of the reed was concentrated at the distal end. Although this scenario does not increase the channel heat flux, it can result in an increase in the amplitude of the reed's oscillation and a reduction in the baseline of the vibration. Consequently, the energy loss decreased from 0.35 to 0.32, leading to an enhancement in the heat transfer efficiency. At this bending stiffness, heat transfer
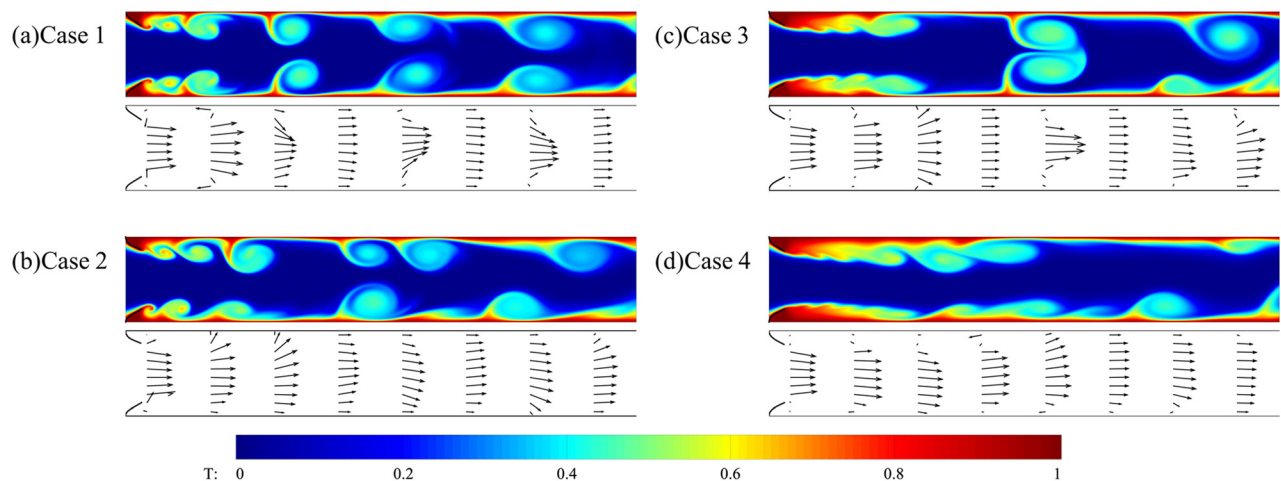
<div style="writing-mode: vertical-rl">08 April 2025 07:26:16</div>

FIG. 5. Temperature field and velocity vector for the four cases ($\gamma = 0.06$).

**TABLE II.** Simulated results for four mass distributions ($\gamma = 0.06$).

Case	$\bar{Q}_{net}$	$\bar{E}_{loss}$	η
Case 1	0.42	0.35	0.89
Case 2	0.42	0.32	0.91
Case 3	0.35	0.36	0.74
Case 4	0.38	0.34	0.81

efficiency increases by 2%. In contrast, cases 3 and 4, as described earlier, have a negative impact on heat transfer in the channel.

B. The influence of bending stiffness

In the previous section, we investigated the influence of different mass distributions on channel heat transfer efficiency when subjected to identical bending stiffness. Our findings revealed that concentrating mass at the distal end of the reed significantly enhances heat transfer efficiency. However, at $\gamma = 0.06$, the improvement in heat transfer effectiveness is relatively weak. To further explore the general applicability of this method under varying bending stiffness and to ascertain if superior results can be achieved, we selected seven bending stiffness values ranging from 0.02 to 0.14. Detailed calculations and analyses were performed for both concentrated mass at the distal end of the reed and uniform mass distribution.

Figure 6 illustrates the relationship between the mass distribution and the average heat flux, average energy loss, and heat transfer efficiency with seven bending stiffness values. We observed that, under both mass distributions, the impact on heat transfer with changing bending stiffness can be roughly categorized into four stages: (1) increase in average heat flux and average energy loss, (2) decrease in average heat flux and increase in average energy loss, (3) decrease in average heat flux and decrease in average energy loss, and (4) increase in average heat flux and decrease in average energy loss. This trend demonstrates that concentrating mass at the distal end of the reed, compared to uniform distribution, exhibits an increase-decrease-increase pattern in heat transfer efficiency as bending stiffness increases, as depicted in Fig. 7. Optimal effectiveness is achieved at a lower bending stiffness, $\gamma = 0.04$, while negative impacts emerge in the bending stiffness range of 0.05–0.10. Beyond $\gamma > 0.10$, the enhancement in heat transfer efficiency continues to increase.
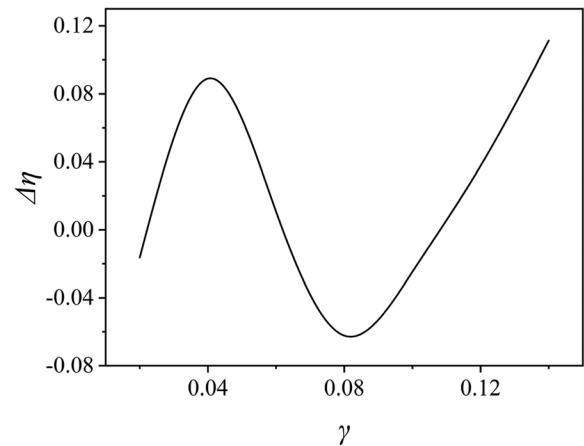
FIG. 7. The difference in heat transfer efficiency between case 1 and case 2 varies with bending stiffness (0.02–0.14).

To analyze the cause of this trend, we initially extracted data regarding the displacement of the reed and assessed its dynamic properties. We examined the oscillation of the reed and the displacement of the reed's distal end along the y-axis, as shown in Fig. 8, as the bending stiffness gradually increased and the mass distribution altered. Comparing the cases of mass concentration at the distal end and uniform mass distribution, we found a clear correlation between the expansion of the motion range and the bending stiffness. For high reed flexibility (e.g., $\gamma = 0.02$), changes in the mass distribution have a relatively minor impact on its motion characteristics. As the bending stiffness gradually increases, the reed with uniform mass distribution begins to exhibit a reduced range of motion. At this point, the advantage of concentrating mass at the distal end of the reed becomes evident, leading to an increase in amplitude, as depicted in Fig. 9. For various bending stiffness values, concentrating mass at the distal end of the reed leads to a decrease in the oscillation frequency while an increase in the amplitude. However, when the bending stiffness ranges from 0.04 to 0.06, the influence of mass distribution on amplitude increase diminishes significantly. This is attributed to increased resistance from the flow field as the bending stiffness increases, which suppresses the reed's oscillation. Additionally, as the bending stiffness surpasses 0.06, the distal end of the reed progressively moves away from the boundary layer, intensifying the flow field's impact.
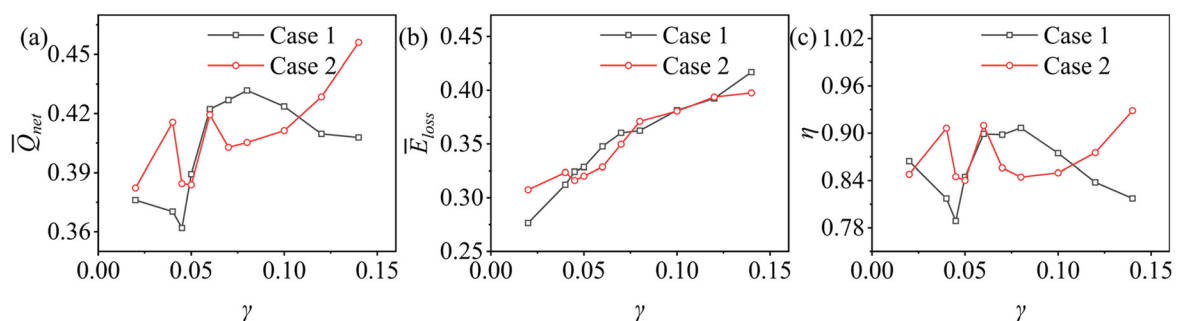
FIG. 6. (a) Mean heat flux, (b) mechanical energy loss, and (c) thermal efficiency factor at case 1 and case 2 ($Re = 400$ and $H/L = 4.0$).
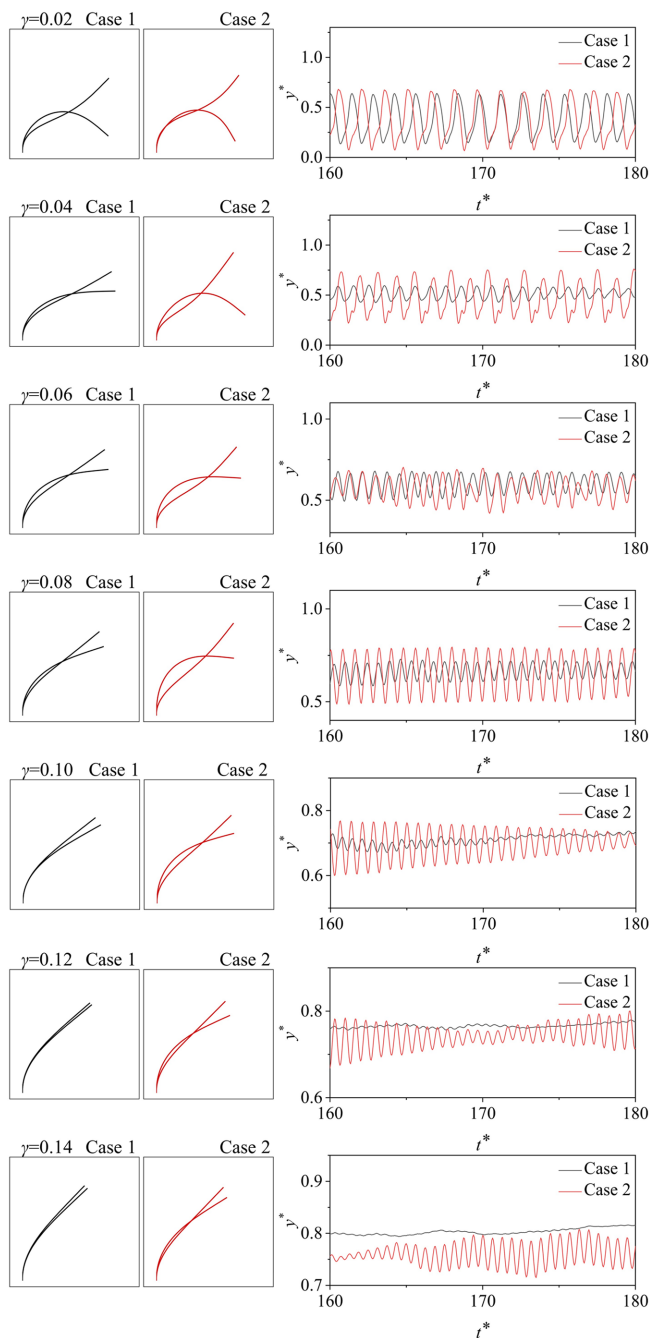
FIG. 8. The range of motion and the temporal evolution of distal end y-axis coordinate of reed under different bending stiffness.

Consequently, concentrating mass at the distal end of the reed results in a significant expansion of the motion range. Notably, when the bending stiffness exceeds 0.12, the reed with uniform mass distribution almost ceases to oscillate, as shown in Fig. 9, the frequency and amplitude tend to be 0, while the reed with mass concentrated at the distal end still has a much obvious amplitude.

From Fig. 6(b), we observed that when the bending stiffness is less than 0.05, changing the mass distribution increased the energy loss of the channel. As shown in Fig. 8, altering the mass distribution increased the amplitude of the reed, which typically leads to an increase in the energy loss of the channel. However, when the bending stiffness is between 0.05 and 0.08, a phenomenon of reduced energy loss after changing the mass distribution emerges. Despite similar increases in the reed's amplitude, different effects on energy loss were observed. To investigate the cause of this phenomenon, we compared the variations in the y-axis coordinates at the distal end of the reed under several bending stiffness conditions, as illustrated in Fig. 10. It was found that although the amplitude of the reed increased under different bending stiffness conditions, the patterns of increase differed. When $\gamma = 0.04$, both the peak and valley of the oscillation were altered, resulting in an increase in the peak and a decrease in the valley, leading to an overall increase in the reed's amplitude, its vibration baseline has not changed. Another pattern emerged when $\gamma = 0.07$, where only the valley of the oscillation was affected, with the peak remaining unchanged and the valley decreased, indicating that the oscillation range of the reed moved closer to the wall. This effectively lowered the baseline of the vibration, which we believe is the reason for the reduced energy loss in the channel. Furthermore, we speculate that this difference is caused by the combined effect of the reed's bending force and the fluid force. With the continuous increase in bending stiffness, the deflection position of the reed moves closer to the center of the channel, where the fluid velocity increases from the wall to the channel center. Consequently, the force exerted by the fluid on the distal end of the reed becomes greater. When the bending force of the reed itself cannot counteract the force exerted by the fluid, concentrating mass at the distal end will lead to an increase in the amplitude of the reed's vibration, while the peak value of the vibration remains unchanged, lowering the baseline of the vibration.

Another issue resides in the fact that, as shown in Fig. 6(a), the alteration of the mass distribution of the reed between bending stiffness values of 0.06 and 0.10 results in a reduction of heat flux within the channel. Previous findings indicate that concentrating the mass of the reed at the distal end led to varying degrees of increased amplitude and decreased oscillation frequency. Both of these phenomena impact the heat flux within the channel. On one hand, an increase in the reed's amplitude leads to an elevation in heat flux; on the other hand, the reduction in oscillation frequency decreases the shedding frequency of vortices, resulting in fewer generated eddies and a subsequent reduction in heat transfer within the channel, leading to a decrease in heat flux. Moreover, our previous analysis revealed that after increasing the bending stiffness, the peak of the reed's oscillation cannot reach higher levels, thus diminishing its effectiveness in increasing heat flux. Based on Fig. 9, we found that under two bending stiffness conditions, $\gamma = 0.02$ and $\gamma = 0.04$, the impact of altered mass distribution on the reed's oscillation amplitude becomes more pronounced. For instance, at $\gamma = 0.02$, the effect on oscillation frequency is almost negligible, while the amplitude increases, leading to the observed increase in heat flux in Fig. 6(a). As the bending stiffness increases, concentrating the mass of the reed at the distal end has an increasingly significant impact on the oscillation frequency, while its influence on the amplitude diminishes. The variation in oscillation frequency has thus become the primary factor affecting heat transfer, as the decrease in oscillation frequency leads to the reduction in heat flux observed at $\gamma = 0.06$ to
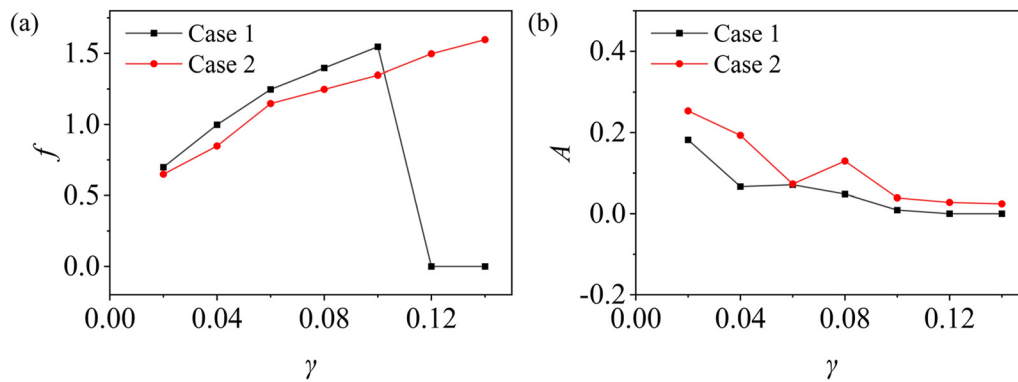
08 April 2025 07:26:16

FIG. 9. (a) Frequency and (b) amplitude of the reed's distal end at various bending stiffness.
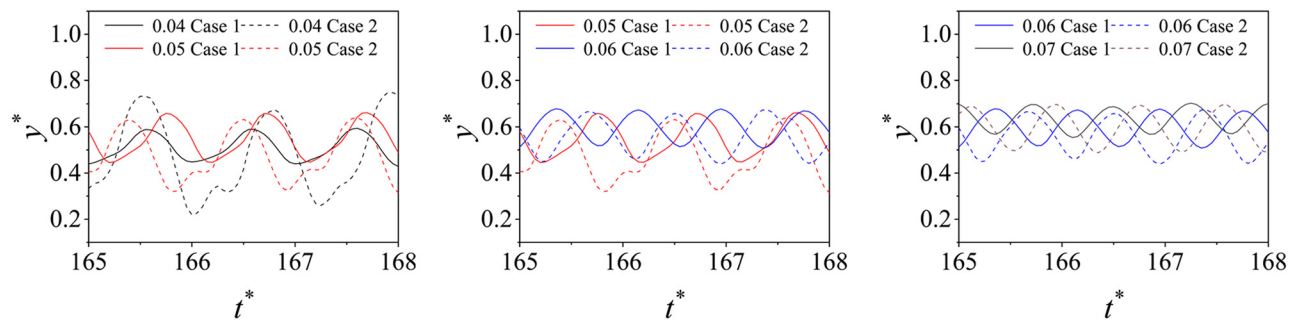

FIG. 10. Time evolution of the y-axis coordinate at the distal end of reed under different bending stiffness (0.04, 0.05, 0.06, 0.07).

$\gamma = 0.10$ in Fig. 6(a). When $\gamma > 0.10$, a uniformly distributed reed exhibits minimal oscillation frequency and amplitude within the channel. However, concentrating its mass at the distal end results in a significant amplitude without a decrease in oscillation frequency, leading to a notable enhancement in heat flux. Subsequently, we will analyze the influence of altering the mass distribution of the reed under different bending stiffness conditions on the temperature field within the channel.

The amplification of reed oscillations under other conditions being constant usually results in a higher average heat flux in the channel. As previously observed for bending stiffness values of 0.04 and 0.14, concentrating mass at the distal end of the reed yielded optimal heat transfer efficiency. Hence, at a specified time point, $t^* = 180$, temperature distribution maps within the channel were generated for these two bending stiffness values (0.04 and 0.14). Additionally, velocity vectors were observed at selected points within the channel, as illustrated in Fig. 11. The figures indicate that the reasons behind the enhanced heat transfer efficiency differ for these two bending stiffness values. For $\gamma = 0.04$, vortices that originally detached unevenly along the wall surface transformed into uniformly detached vortices after concentrating the reed mass at the distal end. These vortices more efficiently conveyed wall heat into the channel, thereby enhancing the heat dissipation capability. Conversely, for $\gamma = 0.14$, the reed, with a uniformly distributed mass, exhibited minimal oscillation due to its lower flexibility, resulting in poor heat transfer with only a few vortices

shedding along the wall. Concentrating the reed mass at the distal end proved advantageous in both cases. With $\gamma = 0.04$, the increased bending stiffness facilitated oscillation, allowing the reed to oscillate closer to the channel center, diverting the trailing vortices away from the wall and toward the channel center. This effectively mixed the wall's heat flow with the cooler flow at the channel center, thereby enhancing heat transfer. In the case of $\gamma = 0.14$, the substantial bending stiffness became an advantage for heat transfer. It enabled the reed to oscillate closer to the channel center, redirecting the trailing vortices away from the wall and toward the channel center, effectively enhancing heat transfer by mixing the wall's heat flow with the cooler flow at the channel center. To study the influence of the time-averaged reed mass distribution on channel temperature distribution, dynamic mode decomposition was performed on temperature fields over 100 time-steps ranging from $t^* = 150$ to 200, as depicted in Fig. 12. It is evident that concentrating the reed mass at the distal end, in the case of $\gamma = 0.04$, according to the 3rd mode of temperature field in case 2, compared with case 1, heat can be better transferred to the channel center, but it still cannot affect the channel center. For $\gamma = 0.14$, the influence of case 1 on the temperature distribution in the channel is localized, whereas case 2 can considerably alter the temperature distribution across the channel, particularly leading to a substantial increase in the temperature at the channel center, thus significantly enhancing the heat transfer. When $\gamma = 0.04$ and $\gamma = 0.14$, the continuity of heat transfer in the channel is improved, the range of change in net heat
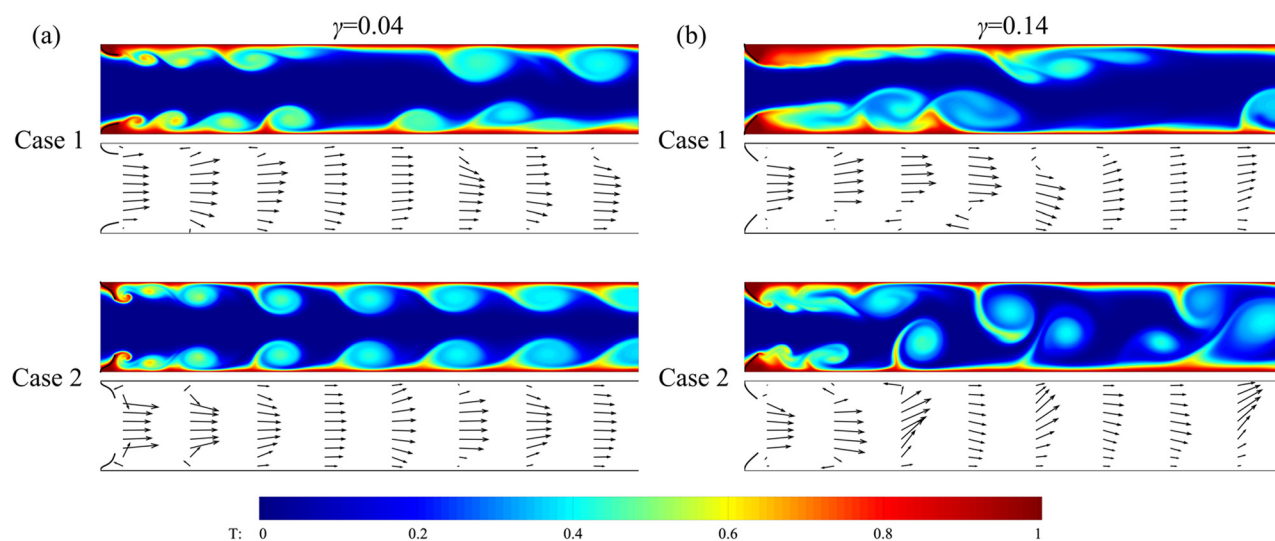
FIG. 11. Temperature field and velocity vector for the two cases under different bending stiffness (a) $\gamma = 0.04$ and (b) $\gamma = 0.14$.
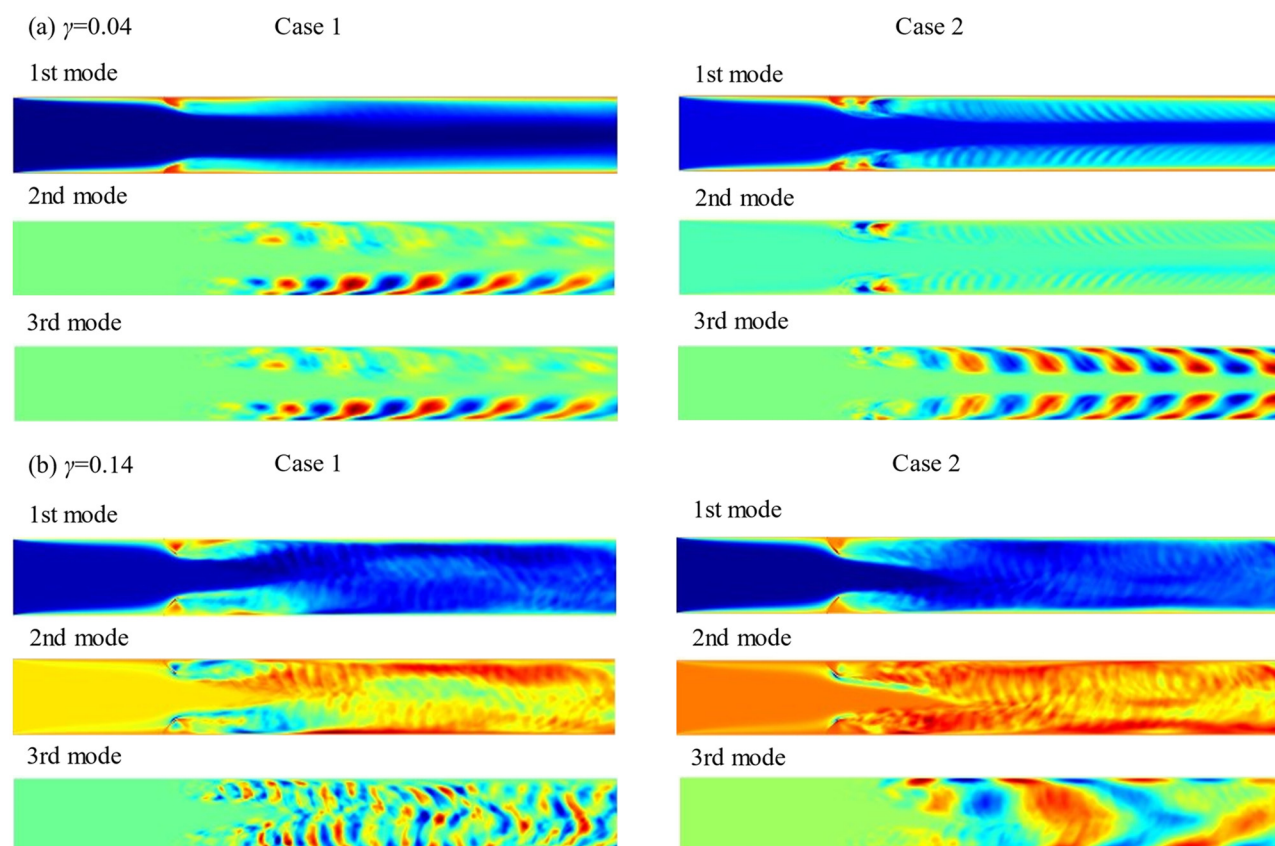

FIG. 12. Dynamic modal decomposition diagram of temperature (a) $\gamma = 0.04$ and (b) $\gamma = 0.14$.
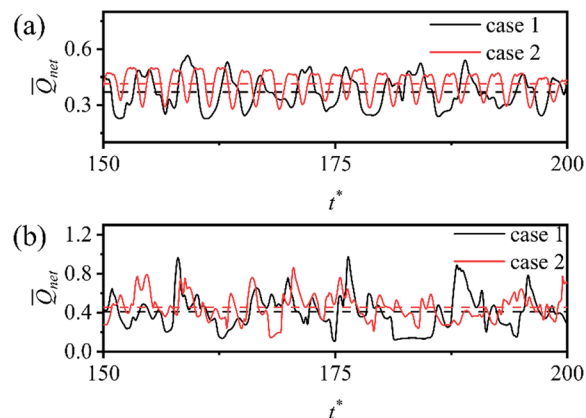
FIG. 13. Heat flux net (a) $\gamma = 0.04$ and (b) $\gamma = 0.14$.

flux decreases, and the average heat flux increases, as depicted in Fig. 13. The temperature field and velocity vector of the two cases with the remaining bending stiffness are depicted in Fig. 14. In the case of $\gamma = 0.02$ with minimal bending stiffness, the temperature field of Case 2 closely resembles that of case 1. For $\gamma = 0.08$ and $\gamma = 0.10$, they represent intermediate transition states. During this phase, case 2 exhibits a detrimental effect compared to case 1. The shedding vortex is closer to the wall, the vortex shedding frequency decreases, and a large area of cold flow occurs in the channel. When $\gamma = 0.12$, case 2 concentrates its mass at the distal end of the reed under the large bending stiffness as analyzed above, and the shed vortices start tending to move toward the center of the channel, contributing to the mixing of the hot flow near the wall and the cold flow in the center of the channel.

VI. CONCLUSIONS

In this study, we conducted a numerical analysis of the impact of four mass distributions of a reed on channel heat transfer efficiency.
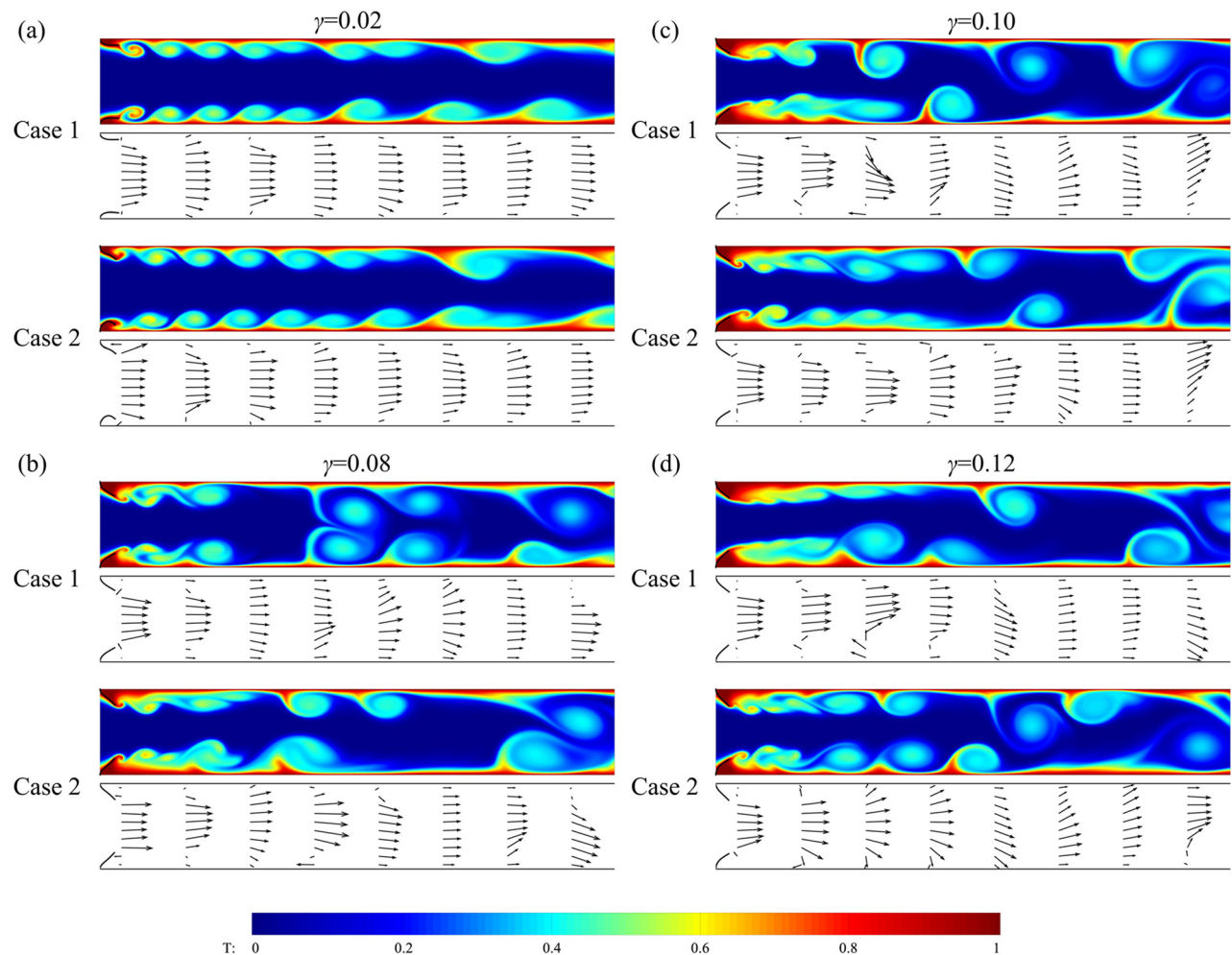

FIG. 14. Temperature field and velocity vector for the two cases under different bending stiffness (a) $\gamma = 0.02$, (b) $\gamma = 0.08$, (c) $\gamma = 0.10$, and (d) $\gamma = 0.12$.

Our findings indicate that the optimal heat transfer efficiency is achieved when mass is concentrated at the distal end of the reed. In the other two cases, a decrease in mass at the distal end leads to a transition in the reed's motion pattern from regular oscillation mode to fully-deflected mode when subjected to flow-induced forces at the distal end. In such instances, heat transfer performance is comparable to that of a rigid body placed on the wall, resulting in a significant decrease in heat transfer efficiency. Therefore, it is recommended to avoid such scenarios in design to enhance heat transfer efficiency.

To delve deeper into the effects of reed mass concentration at the distal end and uniform distribution on channel heat transfer efficiency under varying bending stiffness, simulations were performed for seven bending stiffness values ranging from 0.02 to 0.14. The study analyzed the differences in reed oscillation and their impact on heat transfer efficiency, leading to the following conclusions:

(1) Tuning the mass distribution of the reed to make its mass concentrated at the distal end cannot always enhance heat transfer efficiency across all bending stiffness values; its enhancement effect is closely related to bending stiffness. The impact of reed mass distribution on the heat transfer efficiency exhibits an increasing-decreasing-increasing trend with increasing reed's bending stiffness. At low bending stiffness, concentrating mass at the distal end increases amplitude and generates higher heat flux. However, the increased amplitude results in a higher ratio of reed cross-sectional length to channel width, leading to increased energy losses. In contrast, at high bending stiffness, a uniformly distributed mass prevents reed oscillation. Concentrating mass at the distal end causes the average position of the reed's oscillation to be closer to the wall compared to the reed with uniform mass distribution. This reduces the ratio of reed cross-sectional length to channel width, achieving superior heat transfer performance by simultaneously increasing heat flux and reducing energy losses.

(2) Within the examined bending stiffness range, particularly at $\gamma = 0.04$ and $\gamma = 0.14$, concentrating the reed's mass at the distal end demonstrates the most significant enhancement in heat transfer compared to uniform mass distribution. At $\gamma = 0.04$, increasing amplitude increases vortex shedding frequency, significantly raising heat flux, albeit with increased energy losses. At $\gamma = 0.14$, when concentrating the reed's mass at the distal end, the oscillation range is entirely below the stable position of the reed with uniform mass distribution, reducing energy losses. Additionally, reed oscillation closer to the channel center results in enhanced heat flux, leading to a substantial increase in heat transfer efficiency.

In conclusion, a comprehensive consideration indicates that when the bending stiffness γ reaches 0.04 or exceeds 0.12, concentrating reed's mass at the distal end can improve channel heat transfer efficiency without increasing the overall mass of the cooling system, achieving superior cooling effectiveness.

Considering the complexity of fluid–structure–thermal coupling problems and the computational demands of direct numerical simulations, this study only evaluated a very limited number of linear mass distribution forms. In the future, we hope to use machine learning methods such as physics-informed neural networks (PINNs) to rapidly predict the heat transfer characteristics and reed dynamics of such problems. This approach could enable us to determine more effective mass distribution forms (possibly nonlinear) for the reed to enhance heat transfer.

AUTHOR DECLARATIONS
Conflict of Interest

The authors have no conflicts to disclose.

Author Contributions

Yuzhen Jin: Funding acquisition (lead); Investigation (equal); Project administration (lead); Resources (lead); Supervision (equal); Writing – review & editing (supporting). **Chunhui Leng:** Data curation (lead); Formal analysis (lead); Investigation (equal); Methodology (supporting); Software (equal); Validation (equal); Visualization (lead); Writing – original draft (lead). **Zhaokun Wang:** Methodology (equal); Software (supporting); Writing – review & editing (supporting). **Xuming Zhang:** Project administration (supporting); Resources (equal). **Jingyu Cui:** Conceptualization (lead); Formal analysis (supporting); Funding acquisition (equal); Methodology (lead); Project administration (equal); Supervision (equal); Validation (equal); Writing – review & editing (lead).

DATA AVAILABILITY

The data that support the findings of this study are available from the corresponding author upon reasonable request.

REFERENCES

[1] D.-L. Chen *et al.*, "Assisted heat transfer enhancement in non-Newtonian dielectric fluids based on ion conduction phenomena," Phys. Fluids **35**(11), 113109 (2023).

[2] M. V. Bidari *et al.*, "Effect of triangular perforated flat cone-shaped inserts on performance of double-tube heat exchanger," Phys. Fluids **35**(11), 115133 (2023).

[3] S. S. Mousavi Ajarostaghi *et al.*, "A review of recent passive heat transfer enhancement methods," Energies **15**(3), 986 (2022).

[4] B. Shome, "Slip-flow and heat transfer in microtubes with internal fins," Phys. Fluids **35**(12), 122004 (2023).

[5] L. Zhang *et al.*, "Study of the enhanced heat transfer characteristics of wavy-walled tube heat exchangers under pulsating flow fields," Phys. Fluids **35**(11), 115128 (2023).

[6] X. Sun *et al.*, "Study on the heat transfer enhancement of self-excited oscillating pulsating flow by the boundary vortex group," Phys. Fluids **34**(12), 125122 (2022).

[7] G. Biswas, H. Chattopadhyay, and A. Sinha, "Augmentation of heat transfer by creation of streamwise longitudinal vortices using vortex generators," Heat Transfer Eng. **33**, 406–424 (2012).

[8] L. Shui *et al.*, "The effect of cooling conditions on convective heat transfer and flow in a steam-cooled ribbed duct," J. Mech. Sci. Technol. **28**(1), 331–341 (2014).

[9] D. E. Metzger and S. W. Haley, "Heat transfer experiments and flow visualization for arrays of short pin fins," in Proceedings of the ASME 1982 International Gas Turbine Conference and Exhibit, Heat Transfer; Electric Power Vol. 4 (1982).

08 April 2025 07:26:16

[10]G. I. Mahmood, M. Z. Sabbagh, and P. M. Ligrani, "Heat transfer in a channel with dimples and protrusions on opposite walls," J. Thermophys. Heat Transfer **15**(3), 275–283 (2001).

[11]A. Maji and G. Choubey, "Improvement of heat transfer through fins: A brief review of recent developments," Heat Transfer **49**, 1658 (2020).

[12]F. N. M. Elwekeel, Q. Zheng, and A. M. M. Abdala, "Numerical study of turbulent flow through rib-roughened channels with mist injection," in Proceedings of the ASME Turbo Expo 2014: Turbine Technical Conference and Exposition, Heat Transfer Vol. 5A (2014).

[13]J. Armstrong and D. Winstanley, "A review of staggered array pin fin heat transfer for turbine cooling applications," J. Turbomach. **110**(1), 94–103 (1988).

[14]S. Caliskan et al., "Experimental investigation of the effect of flexible/rigid flag on heat transfer," Int. J. Therm. Sci. **188**, 108147 (2023).

[15]K. Shoele and R. Mittal, "Computational study of flow-induced vibration of a reed in a channel and effect on convective heat transfer," Phys. Fluids **26**(12), 127103 (2014).

[16]J. B. Lee et al., "Heat transfer enhancement by flexible flags clamped vertically in a Poiseuille channel flow," Int. J. Heat Mass Transfer **107**, 391–402 (2017).

[17]J. B. Lee, S. G. Park, and H. J. Sung, "Heat transfer enhancement by asymmetrically clamped flexible flags in a channel flow," Int. J. Heat Mass Transfer **116**, 1003–1015 (2018).

[18]Y. Chen et al., "Heat transfer enhancement in a Poiseuille channel flow by using multiple wall-mounted flexible flags," Int. J. Heat Mass Transfer **163**, 120447 (2020).

[19]Y. Chen et al., "Flapping dynamics of vertically clamped three-dimensional flexible flags in a Poiseuille flow," Phys. Fluids **32**, 071905 (2020).

[20]Y. D. Jeong et al., "Heat transfer enhancement in a channel flow using two wall-mounted flexible flags with a confined cylinder," Int. J. Heat Mass Transfer **195**, 123185 (2022).

[21]S. G. Park, "Heat transfer enhancement by a wall-mounted flexible vortex generator with an inclination angle," Int. J. Heat Mass Transfer **148**, 119053 (2020).

[22]W. Jiansheng, W. Xin, and L. Xueling, "Numerical investigation on flow behavior and heat transfer feature of flexible wings located at the bottom of a two-dimensional channel," Appl. Therm. Eng. **206**, 118112 (2022).

[23]M. S. Kang, S. G. Park, and C. T. Dinh, "Heat transfer enhancement by a pair of asymmetric flexible vortex generators and thermal performance prediction using machine learning algorithms," Int. J. Heat Mass Transfer **200**, 123518 (2023).

[24]A. Dadvand et al., "Enhancement of heat and mass transfer in a microchannel via passive oscillation of a flexible vortex generator," Chem. Eng. Sci. **207**, 556–580 (2019).

[25]A. Goza, "Flow-induced flapping of an inverted flag with non-uniform stiffness distribution," in AIAA SCITECH 2022 Forum (American Institute of Aeronautics and Astronautics, 2021).

[26]C. S. Peskin and D. M. McQueen, "Computational biofluid dynamics," Contemp. Math. **141**, 161–186 (1993).

[27]W.-X. Huang, S. J. Shin, and H. J. Sung, "Simulation of flexible filaments in a uniform flow by the immersed boundary method," J. Comput. Phys. **226**(2), 2206–2228 (2007).

[28]B. S. H. Connell and D. K. P. Yue, "Flapping dynamics of a flag in a uniform stream," J. Fluid Mech. **581**, 33–67 (2007).

[29]L. Zhu and C. Peskin, "Simulation of a flapping flexible filament in a flowing soap film by the immersed boundary method," J. Comput. Phys. **179**, 452–468 (2002).

[30]F. B. Tian et al., "An efficient immersed boundary-lattice Boltzmann method for the hydrodynamic interaction of elastic filaments," J. Comput. Phys. **230**(19), 7266–7283 (2011).

[31]J. Ryu, S. G. Park, and H. J. Sung, "Flapping dynamics of inverted flags in a side-by-side arrangement," Int. J. Heat Fluid Flow **70**, 131–140 (2018).

[32]L. Zhu and C. S. Peskin, "Interaction of two flapping filaments in a flowing soap film," Phys. Fluids **15**(7), 1954–1960 (2003).

[33]L. Zhu, "Simulation of an inhomogeneous elastic filament falling in a flowing viscous fluid," Phys. Fluids **19**(1), 017113 (2007).

[34]C. S. Peskin, "Numerical analysis of blood flow in the heart," J. Comput. Phys. **25**(3), 220–252 (1977).

[35]Z. Guo, B. Shi, and C. Zheng, "A coupled lattice BGK model for the Boussinesq equations," Numer. Methods Fluids **39**, 325–342 (2002).

[36]S. Hosseini et al., "An immersed boundary-lattice Boltzmann method with multi relaxation time for solving flow-induced vibrations of an elastic vortex generator and its effect on heat transfer and mixing," Chem. Eng. J. **405**, 126652 (2021).

[37]Z. Wang, Y. Wei, and Y. Qian, "A simple direct heating thermal immersed boundary-lattice Boltzmann method for its application in incompressible flow," Comput. Math. Appl. **80**(6), 1633–1649 (2020).

[38]X. D. Niu et al., "A momentum exchange-based immersed boundary-lattice Boltzmann method for simulating incompressible viscous flows," Phys. Lett. A **354**(3), 173–182 (2006).

[39]J. Cui, Y. Liu, and Y. Jin, "Impact of initial fiber states on different fiber dynamic patterns in the laminar channel flow," Int. J. Mech. Sci. **198**, 106359 (2021).

[40]J. Cui et al., "Numerical simulation of fiber conveyance in a confined channel by the immersed boundary-lattice Boltzmann method," Eur. J. Mech. B Fluids **76**, 422–433 (2019).

[41]Y. Jin, Y. Liu, and J. Cui, "Numerical study on the motion characteristics of an elastic fiber migrating in a cylindrical Couette flow with centrifugal effect," Acta Mech. Sin. **39**(3), 322423 (2023).

[42]S. G. Park et al., "Simulation of fluid-flexible body interaction with heat transfer," Int. J. Heat Mass Transfer **110**, 20–33 (2017).